BABAKHANI, Peyman <http://orcid.org/0000-0002-5318-4320>, BRIDGE, Jonathan <http://orcid.org/0000-0003-3717-519X>, PHENRAT, Tanapon <http://orcid.org/0000-0003-2179-042X>, FAGERLUND, Fritjof, DOONG, Ruey-an and WHITTLE, Karl R <http://orcid.org/0000-0002-8000-0857>

Citation:

Comparison of a new mass-concentration, chain-reaction model with the population-balance model for early- and late-stage aggregation of shattered graphene oxide nanoparticles

Peyman Babakhani,[1,2,3]* Jonathan Bridge,[4] Tanapon Phenrat,[5,6] Fritjof Fagerlund,[7] Ruey-an Doong,[2,8] Karl R Whittle[2]**

[1]Earth Surface Science Institute, School of Earth and Environment, University of Leeds, Leeds LS2 9JT, UK
[2]School of Engineering, University of Liverpool, Liverpool, Merseyside L69 3GH, UK
[3]Department of Biomedical Engineering and Environmental Sciences, National Tsing Hua University, No. 101, Section 2, Kuang Fu Road, Hsinchu, 30013, Taiwan
[4]Department of the Natural and Built Environment, Sheffield Hallam University, Howard St, Sheffield S1 1WB, UK
[5]Research Unit for Integrated Natural Resources Remediation and Reclamation (IN3R), Department of Civil Engineering, Faculty of Engineering, Naresuan University, Phitsanulok, Thailand, 65000
[6]Center of Excellence for Sustainability of Health, Environment and Industry (SHE&I), Faculty of Engineering, Naresuan University, Phitsanulok, Thailand, 65000
[7]Department of Earth Sciences, Uppsala University, Villavägen 16, 75236 Uppsala, Sweden
[8]Institute of Environmental Engineering, National Chiao Tung University, No. 1001, University Road, Hsinchu, 30010, Taiwan

*Corresponding author:
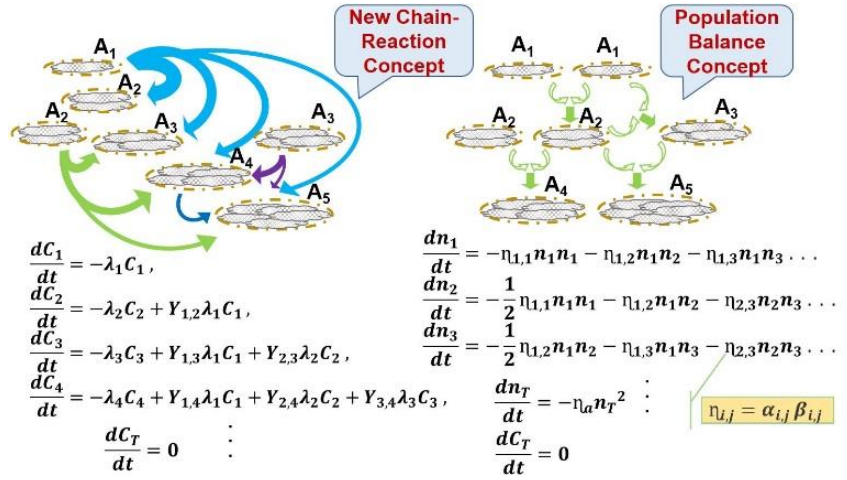
T: +44(0)7913000434, emial: p.babakhani@leeds.ac.uk

** Corresponding author:

T: +44(0)1517944680, emial: Karl.Whittle@liverpool.ac.uk

1

$$\frac{dC_1}{dt} = -\lambda_1 C_1,$$
$$\frac{dC_2}{dt} = -\lambda_2 C_2 + Y_{1,2}\lambda_1 C_1,$$
$$\frac{dC_3}{dt} = -\lambda_3 C_3 + Y_{1,3}\lambda_1 C_1 + Y_{2,3}\lambda_2 C_2,$$
$$\frac{dC_4}{dt} = -\lambda_4 C_4 + Y_{1,4}\lambda_1 C_1 + Y_{2,4}\lambda_2 C_2 + Y_{3,4}\lambda_3 C_3,$$
$$\frac{dC_T}{dt} = 0$$

$$\frac{dn_1}{dt} = -\eta_{1,1}n_1 n_1 - \eta_{1,2}n_1 n_2 - \eta_{1,3}n_1 n_3 \cdots$$
$$\frac{dn_2}{dt} = -\frac{1}{2}\eta_{1,1}n_1 n_1 - \eta_{1,2}n_1 n_2 - \eta_{2,3}n_2 n_3 \cdots$$
$$\frac{dn_3}{dt} = -\frac{1}{2}\eta_{1,2}n_1 n_2 - \eta_{1,3}n_1 n_3 - \eta_{2,3}n_2 n_3 \cdots$$
$$\frac{dn_T}{dt} = -\eta_a n_T^2$$
$$\frac{dC_T}{dt} = 0$$
$$\eta_{i,j} = \alpha_{i,j}\beta_{i,j}$$

31

32

Graphical Abstract

34

Abstract

Aggregation as an essential mechanism impacting nanoparticle (NP) functionality, fate, and transport in the environment is currently modelled using population-balance equation (PBE) models which are computationally expensive when combined with other continuum-scale reactive transport models. We propose a new simple mass-concentration-based, chain-reaction modelling (CRM) framework to alleviate computational expenses of PBE and potentially to facilitate combination with other fate, transport, and reaction models. Model performance is compared with analytical PBE solution and a standard numerical PBE technique (fixed pivot, FP) by fitting against experimental data (i.e., hydrodynamic diameter and derived count rate of dynamic light scattering used as a representative of mass concentration) for early- and late-stage, aggregation of shattered graphene oxide (SGO) NP across a broad range of solution

2

chemistries. In general, the CRM approach demonstrates a better match with the experimental data with a mean Nash-Sutcliffe model efficiency (NSE) coefficient of 0.345 than the FP model with a mean NSE of 0.29. Comparing model parameters (aggregation rate constant and fractal dimension) obtained from fitting CRM and FP to the experimental data, similar trends or ranges are obtained between the two approaches. Computationally, the modified CRM is an order-of-magnitude faster than the FP technique, suggesting that it can be a promising modelling framework for efficient and accurate modelling of NP aggregation. However, in the scope of this study, reaction rate coefficients of the CRM have been linked to collision frequencies based on simplified and empirical relationships which need improvement in future studies.

Keywords: Nanoparticles, environmental fate and transport, early and late aggregation, sedimentation, chain reaction model, mass concentration

1   Introduction

Production of nanomaterials is now a mainstream commercial industry. For example, graphene oxide (GO) nanosheets with 12 morphologies are routinely manufactured across 40 countries, within 15 industries, and 585 applications [1, 2]. Commercial waste streams can lead to uncontrolled spread of nanomaterials in the environment [3, 4], however, there is also a range of opportunities for the use of nanomaterials in environmental systems, e.g., environmental applications such as clean-up of radionuclide contaminated sites [5-8], agronomic applications such as the use as nano-fertilizers and nano-pesticides [9, 10], and petroleum applications such as oil/gas reservoir recovery enhancement [11, 12]. It is of paramount importance to predict and control the

3

70   interactions, reactions, transport, and fate of nano-particulates in aquatic environments, a

71   task which is already a key challenge for water and environmental engineers.

72   One of the critical phenomena that controls NP fate and transport as well as their

73   reactions and functionality in environmental and engineering systems is aggregation [12-

74   21]. Efficient integration of aggregation models with other NP fate, transport, and

75   reaction models is crucial to enable the estimation of NP release into aquatic

76   environments and designing NP application strategies [22-24]. Such models include:

77   continuum models, i.e., advection-dispersion-reaction equations describing bulk mass

78   transport over continuous spatial domains [21, 25, 26], NP life cycle assessment (LCA)

79   which is a comprehensive modelling framework used to assess environmental and

80   human health impacts of nanomaterials [27, 28], and abstract models including material

81   flow analysis (MFA) or multi-media models (MMM) which are based on the mass

82   balance principle at global and local scales [3, 29-32].

83   Recent investigation of the NP aggregation within systems such as porous media

84   and surface waters revealed the need for further development of aggregation models to

85   take realistic environmental complexity arisen from local particle resuspension into

86   account [15]. There are several complex interactions which require consideration in a

87   reactive transport model along with aggregation including NP reaction with existent

88   pollutants [33, 34], interaction with background colloids and natural organic matter

89   (hetero-aggregation), [16, 35-37], and with porous media [21, 25], as well as NP

90   dissolution, sulfidation, and sedimentation [38-40]. Modelling approaches to aggregation

91   with various levels of accuracy and efficiency are already available which are mostly

92   different adaptations of PBE models [22, 40-42]. Yet a flexible, efficient, and accurate

93   aggregation model that can be simply adapted and be coupled with other multiple-

94   constituent models of NP fate, transport, and reaction, which are already computationally

4

95 expensive, [43-45] is lacking. Furthermore, it is desirable for an aggregation model to be

96 based on mass concentration as consistency of their main state variable with most of

97 other models may facilitate their combination and since experimental/field data used as

98 their input are also more readily available in terms of mass concentration [24].

99   In this study, we present a simple mass-concentration-based approach with the aim

100 to model aggregation more efficiently than common PBE, with an improved or similar

101 accuracy. A modified chain reaction model (CRM) which is based on the mass

102 concentration, may be capable of accounting for dynamics of the aggregate populations

103 by resembling each particle size class as a species of the reaction. We propose that such

104 a model may be a better alternative to PBE for integration with other NP fate, transport,

105 and reaction models due to similarity in formulation to conventional reaction equations,

106 potential computational efficiency, and flexibility in formulation and size classification.

107 Fundamentally, an aggregation model generally follows a second order expression if

108 described in terms of particle number concentration [46-48]. For pure aggregation, this

109 expression leads to a decay in the number concentration of primary particles and the total

110 number concentration over time while the total mass concentration is constant

111 theoretically. Likewise, a mass concentration-based model should be able to describe

112 mass transfer among classes of the aggregates while maintaining the total mass constant.

113 The CRM is based on a series of first-order decay expressions maintaining the total mass

114 in the system constant. We investigate whether this approach, after being compared with

115 analytical solution of the PBE [49, 50], can describe the change in mean particle size,

116 PSD, and concentration of shattered graphene oxide (SGO) NP under quiescent

117 conditions of aggregation and sedimentation across a range of solution chemistries

118 including different electrolyte concentrations, electrolyte species, and pH. We also

119 compare the model performance with a typical PBE, i.e., the FP technique [51] which

120 has been widely used as a standard approach for comparison with other models [52-54].

121 To the best of our knowledge this is the first time that a mass-concentration CRM-based

122 formulation is used for modelling the aggregation of colloidal particles. The previous use

123 of the terminology 'parallel parent and daughter' in the literature of particle aggregation

124 [55] was associated with the discretization of the PBE model.

2 Model Development

126 The basic CRM which has long been used in the context of dissolved contaminant

127 transport in groundwater is as follows [56-58]:

$$\frac{dC_k}{dt} = L(C_k) - \lambda_k C_k + Y_{k-1,k} \lambda_{k-1} C_{k-1} \tag{1}$$

128   If $k = 1$:

$$\frac{dC_1}{dt} = L(C_1) - \lambda_1 C_1 \tag{2}$$

129   where C_k is mass concentration [ML^{-3}] of species k, $L(C_k)$ stands for the non-

130 reaction terms including other transport mechanisms such as advection, dispersion, fluid

131 sinks/sources, and/or sedimentation; λ_k is the first-order reaction coefficient [T^{-1}] for

132 species k, and $Y_{k-1,k}$ is the yield coefficient [–] between species k-1 and k, which for

133 physical chain-reaction models can be calculated from the stoichiometric relationship

134 between the two species [57].

135   To apply this concept to aggregation mechanisms, we first assume that particle

136 volume/size dimension discretisation is regular and sequential based on a geometric

137 series given as $v_{i+1}/v_i = 2^{1/q}$, where q is the geometric factor and v is volume of each

138 size class. Hence, size class k can have multiple additional primary particles compared to

139 size class k-1. This is already a common assumption in the context of population balance

6

140　modelling [40, 59, 60]. Considering the aforementioned basic CRM for such a size

141　discretization means that when particles of size class k-1 aggregate with each other and

142　with particles of smaller size classes, the mass concentration of their class, k-1, decays

143　and the mass concentration of one size class larger, k, increases. Based on this concept

144　and disregarding the term, $L(C_k)$ in Eq. (1), i.e., considering pure aggregation, one needs

145　to assume $Y_{k-1,k} = 1$, in order to maintain the total mass of all size classes constant. This

146　model, however, may only consider the aggregation of size class k-1 and smaller classes

147　resulting in creation of mass in only class k. Although due to the geometric nature of

148　size classification, size class k can be sufficiently larger than its lower size class to

149　accommodate aggregates produced in this way, a more accurate approach may be that

150　aggregation of size class k-1 and smaller classes results in redistribution of mass from

151　class k-1 among several larger classes. Therefore, we modify the basic form of the CRM

152　model as follows:

$$\frac{dC_k}{dt} = L(C_k) - \lambda_k C_k + \sum_{i=1}^{k-1} Y_{i,k} \lambda_i C_i \tag{3}$$

153　　　where k is the aggregate class size for which Eq. (3) is being solved. Since in the

154　aggregation process first smaller aggregates are formed and then larger ones after

155　collisions of the formers, the probability for transformation into larger classes should

156　decrease with the increase in size class. We assume that $Y_{i,k}$ can be expressed as a linear

157　function of volumes of size classes, which are already geometrically distributed, and

158　considering total sum of $Y_{i,k}$ equal to one:

$$Y_{i,k} = \frac{v_{k_{max}-k+i+1}}{\sum_{j=i+1}^{k_{max}} v_j} \tag{4}$$

7

159   where k_{max} is the maximum number of classes considered in the model, and v is

160   the volume of each class. For instance, assuming $k_{max} = 5$ and combining both Eqs. (3)

161   and (4) yields:

$$\frac{dC_1}{dt} = -\lambda_1 C_1 ,$$

k=1

$$\frac{dC_2}{dt} = -\lambda_2 C_2 + \frac{v_5}{v_2 + v_3 + v_4 + v_5} \lambda_1 C_1 ,$$

k=2

$$\frac{dC_3}{dt} = -\lambda_3 C_3 + \frac{v_4}{v_2 + v_3 + v_4 + v_5} \lambda_1 C_1 + \frac{v_5}{v_3 + v_4 + v_5} \lambda_2 C_2 ,$$

k=3

$$\frac{dC_4}{dt} = -\lambda_4 C_4 + \frac{v_3}{v_2 + v_3 + v_4 + v_5} \lambda_1 C_1 + \frac{v_4}{v_3 + v_4 + v_5} \lambda_2 C_2$$

$$+ \frac{v_5}{v_4 + v_5} \lambda_3 C_3 ,$$

k=4

$$\frac{dC_5}{dt} = \frac{v_2}{v_2 + v_3 + v_4 + v_5} \lambda_1 C_1 + \frac{v_3}{v_3 + v_4 + v_5} \lambda_2 C_2 + \frac{v_4}{v_4 + v_5} \lambda_3 C_3$$

$$+ \frac{v_5}{v_5} \lambda_4 C_4 ,$$

k=5

162   Since in the present study we only consider sedimentation along with aggregation,

163    $L(C_k)$ is given as [40, 61]:

$$L(C_k) = -\frac{U_k}{Z_s} C_k \tag{5}$$

164   where Z_s is the sedimentation depth [L] and U_k is the sedimentation velocity of

165   aggregates in class k [LT^{-1}] given as [62]:

$$U_k = \frac{g}{18\mu}(\rho_0 - \rho_w)(2a_0)^{3-D_f}(2a_k)^{D_f-1} \tag{6}$$

166   where g is the gravitational acceleration, ρ_0 is the density of primary particles, [ML^{-3}],

167   ρ_w is the density of water [ML^{-3}], μ is the dynamic viscosity of the suspending medium

8

168   [M T^{-1} L^{-1}], a_0 is the primary particle radius [L], a_k is an aggregate radius in size class k

169   [L], and D_f is the fractal dimension.

170   Reaction coefficients, λ_k, should be expressed in a way that they incorporate the

171   nature of collision analogous to the conventional Smoluchowski model [63]. Here as a

172   first study developing a CRM framework, we propose two different simplifying

173   approaches to describe λ_k. For the first approach we rely on particle sizes, analogous to

174   the so-called 'sum' collision frequency commonly used in population balance modelling

175   [52, 64]. Such a size-based semi-empirical equation, hereafter designated as S-CRM,

176   may be expressed as follows:

$$\lambda_k = \frac{\Lambda_S}{\tau}\left(\frac{\left|a_{k_{max}-k+1} - a_{ave,t}\right|}{a_k}\right)^{\psi}, \qquad 2 \le k \le k_{max} \qquad (7)$$

177   where Λ_S is the aggregation constant of the S-CRM, mimicking the attachment efficiency

178   in population-balance models, $a_{ave,t}$ is the equivalent radius of the geometric mean size of

179   PSD at time t, ψ is an empirical power which depends on the size discretization

180   approach and is assumed in the present study to be 0.5, and τ is the characteristic time

181   [T] of aggregation (coagulation time or aggregation half-life) given as follows [46]:

$$\tau = \frac{3\mu}{4k_b T n_0} \qquad (8)$$

182   where k_b is the Boltzman constant, μ is the viscosity of the suspending medium [M T^{-1}

183   L^{-1}], T is temperature [K], n_0 is the initial population of particles which can be

184   determined from the initial PSD. Equation (7) is based on this concept that the rate of

185   aggregation, λ_k, may vary with the size of class in respect to the geometric-average size

186   of the PSD [40]. When the geometric mean size of the aggregates grows during the

187   aggregation process, the rates may also change for each class of particle over time.

188   Therefore, the rates are updated in every time steps of the numerical solution. The

189 variation of λ_k over time through $a_{ave,t}$ might help better constraining the dynamic

190 cascading aspect of the aggregation if the model is applied in realistic environmental

191 condition [15]. It should be noted that this model considers the Brownian motion through

192 τ, such that increasing temperature and decreasing size can promote λ_k thereby the

193 aggregation rate. This model may also consider the differential sedimentation

194 mechanism of aggregation with larger differences between particles and $a_{ave,t}$ yielding

195 larger λ_k. To clarify this, the following example is given considering a maximum

196 number of size classes as five:

$$\lambda_2 = \frac{\Lambda_S}{\tau}\left(\frac{|a_4 - a_{ave,t}|}{a_2}\right)^{1/2} \qquad \text{k=2}$$

$$\lambda_3 = \frac{\Lambda_S}{\tau}\left(\frac{|a_3 - a_{ave,t}|}{a_3}\right)^{1/2} \qquad \text{k=3}$$

$$\lambda_4 = \frac{\Lambda_S}{\tau}\left(\frac{|a_2 - a_{ave,t}|}{a_4}\right)^{1/2} \qquad \text{k=4}$$

$$\lambda_5 = \frac{\Lambda_S}{\tau}\left(\frac{|a_1 - a_{ave,t}|}{a_5}\right)^{1/2} \qquad \text{k=5}$$

197 Alternatively, in the second approach to account for variations in λ_k across size

198 classes, we directly utilize the concept of collision frequencies from the Smoluchowski

199 model [63, 65]. However, instead of taking all possible collisions into account, we

200 assume two types of collisions are dominant among all possible collisions. These include

201 collisions between particles of similar size and collisions between any given particles

202 and a particle with a geometrical mean size of PSD [66, 67]. By adding these two types

203 of collision frequencies and nondimensionalizing each term by the maximum of their

204 range, the following expression is resulted which is hereafter designated as C-CRM:

10

$$\lambda_k = \frac{\Lambda_C}{\tau} \left(\frac{\beta_{k,k}}{\beta_{1,1}} + \frac{\beta_{k,k_{ave}}}{\beta_{k_{max},k_{ave}}} \right) \tag{9}$$

205   where Λ_C is the aggregation constant of the C-CRM, $\beta_{k,k}$ is the collision frequency

206   between each class of aggregates and classes of the same size; $\beta_{k,k_{ave}}$ is the collision

207   frequency between each class of aggregates and the class that has an equivalent size with

208   the geometric mean size of the PSD in each time step; $\beta_{1,1}$ and $\beta_{k_{max},k_{ave}}$ are the

209   maximum of $\beta_{k,k}$ and $\beta_{k,k_{ave}}$ ranges, respectively, for all size classes. Calculations of

210   these collision frequencies with considering all three aggregation mechanisms (i.e.,

211   Brownian, differential sedimentation, and orthokinetic aggregations) have been

212   presented previously [40, 46] and are also available in the Supporting Information (SI).

213   These equations are all expressed based on aggregate volumes to avoid the impact of

214   aggregate shape on model outcomes [68]. It should be mentioned that

215   nondimensionalizing each type of collision rate by the maximum of their range in Eq. (9)

216   causes ignorance of the role of the two collision types in relation to each other. This may

217   not be important in the scope of the present paper which aims to investigate whether the

218   general formulation of CRM with simplifying assumptions about calculation of model

219   coefficients can describe aggregation of NP.

220   We compared the performances of the models with an accurate population balance

221   model solution known as the FP scheme [51] given as:

$$\frac{dn_k}{dt} = \sum_{\substack{j,i \\ v_{k-1} \leq (v_j+v_i) \leq v_{k+1}}}^{j \geq i} \left[1 - \frac{1}{2} \delta_{j,i} \right] \eta_k \alpha \beta_{j,i} \, n_j n_i \; - n_k \sum_{i=1}^{k_{max}} \alpha \, \beta_{k,i} \, n_i - \frac{U_k}{Z_s} n_k \tag{10}$$

222   where η_k is:

11

$$\eta_k = \begin{cases} \dfrac{v_{k+1}-(v_j+v_i)}{v_{k+1}-v_k}, & v_k \leq (v_j + v_i) \leq v_{k+1} \\ \\ \\ \dfrac{(v_j+v_i)-v_{k-1}}{v_k-v_{k-1}}, & v_{k-1} \leq (v_j + v_i) \leq v_k \end{cases} \tag{11}$$

223   where n_k is particle number concentration of aggregates in size class k $[L^{-3}]$, v_i is the

224   volume of solids in each aggregate in size class i, δ is Kronecker delta, and α is the

225   attachment efficiency which is typically estimated as an aggregation constant through

226   model fitting to experimental data. A code written in MATLAB© (Version 2016a,

227   Mathworks, USA) was used and modified for solving this study's models, the details of

228   which are summarised in the SI and are available in Babakhani et al. [40]. Briefly, an

229   explicit forward Euler scheme was used for the time discretization of Eqs. (3) and (10)

230   with an adjustable time-step. A power-law model [62, 69] was used for settling velocity

231   and the Brinkman permeability model [40, 70, 71] was used to calculate permeability in

232   collision frequency formulation. This model set was already found to best describe early

233   and late stages of aggregation and sedimentation of hydroxyapatite (HAp) NP among 24

234   model combinations [40]. Particle size distribution observed in the beginning of each

235   experiment was used as the initial condition in the aggregation model.

236   The optimization algorithm code developed in the former study [40] was also used here

237   for calibration of parameters including aggregation constant (Λ in CRM or α in PBE)

238   which controls the aggregation rate and fractal dimension (D_f) which controls the

239   sedimentation velocity through Eq. (6) and collision frequencies through Eqs. (S1-S3).

240   Adjusting both parameters was necessary to fit the model against experimental data of

241   both early and late stages of aggregation as demonstrated in the previous study [40]. All

242   simulation characteristics were the same for different modelling approaches. The Nash–

Sutcliffe model efficiency (NSE) coefficient [72] was used to compare different model performances against experimental data and analytical solution outputs. To calculate the mass balance, masses of particles remained suspended were integrated at the end of the simulation and was added to the integration of all mass fractions removed in each time step in a given cell at the end of simulation. The difference between this total mass and the initial mass put in the system divided by the initial mass was reported as the mass balance error. The analytical solution used for comparison with the new CRM was based on a log-normal distribution initial PSD. These are described in detail in the SI. In order to compare the CPU runtimes for different models, the models were run on a 64-bit Operating System with 3.5 GHz Intel® Xeon® CPU and 32 GB RAM.

3 Experimental

Graphene oxide (particle density 1.8 g/cm^3) was obtained from Siniocarbon, China, in powder form and dispersed in deionized (DI) water at 2 g/L. Shattered graphene oxide was then produced via intensive ultra-sonication of the GO dispersion to achieve a relatively uniform initial hydrodynamic diameter of 90 nm. This was accomplished using a probe sonication at an amplitude of 30 µm and power of 40 W for 2 h with 30-second stop following each 30-second sonication. The dispersion was then centrifuged for 30 min at 19500 $\pm$ 500 rpm to remove the fraction of larger particles. Finally, the dispersion was passed through a 0.45 μm syringe filter and the filtrate was kept in dark at 4 ℃ as the stock dispersion. The concentration of this dispersion was determined using gravimetric measurement and was adjusted at the set concentration (50 mg/L) before each aggregation experiment.

The evolution of aggregate size and concentration was measured over the course of each experiment at intervals of ~3.4 min using Dynamic Light Scattering (DLS)

13

technique (Malvern Zetasizer Nano ZS, UK) as this has been used for characterizing non-spherical particles/aggregates frequently [73-75]. The valid measurement size range reported by the manufacturer is 1 nm to 10^4 nm. The same instrument was used for measuring the zeta potential. The instrument settings for size measurement were fixed for all measurements following Babakhani et al. [40]. These include using 5 runs each with a duration of 10 s for every measurement, setting the beam attenuator at a unit of 11, and the position of measurement at 6.5 mm. All experiments were conducted in duplicate for a duration >5 h. The standard deviations of the duplicate tests are reported as error bars in the final plots [76-78]. A sample volume of 3 mL was used inside the cuvette for all cases, corresponding to the measurement depth of ~2.3 cm and total water column height of ~3 cm. For fitting the model outputs we used the hydrodynamic diameter (D_H), a scattered light intensity mean also known as cumulant mean, along with the derived count rate (DCR) data used as an indicator of mass concentration [40, 79, 80]. Derived count rate was measured at different concentrations (5, 50, 500, and 1000 mg/L) of SGO to examine the correlation between the two quantities. The model fitted to D_H and DCR data was then used to describe experimental PSD obtained in the middle (150 min) and the end of each experiment (300 min). For PSD data a volume-based distribution was used, and the analysis model of the Zetasizer software was selected as "General Purpose (Normal Resolution)".

All experiments were conducted according to the following procedure: (1) prepare the particle dispersion in DI water for a final particle concentration of 50 mg/L; (2) adjust the pH at 6 ± 0.05 (or alternatively at 2.5, 4, 7.5, or 10) with NaOH/HCl (100 mM); (3) ultrasonication for 5 min, add the electrolyte (either $NaClO_4$ or $CaCl_2$), immediately vortex for 5 s, transform to a disposable cuvette, and immediately start the measurement. The whole process after taking from ultrasonicator until the start of the

14

292 first measurement took 70 ± 20 s. The pH set for different cases did not show

293 considerable variations over the course of experiment; with maximum variation for pH

294 7.5 decreasing to 7.1 after ~15 h.

4   Results and discussion

4.1   Comparison of the chain-reaction model with the analytical solution

297 Before assessing the CRM against experimental results, we first theoretically compare

298 CRM's performance with the analytical solution of the population balance model. Since

299 the aggregation rate constants of S-CRM and C-CRM, Λ_S and Λ_C, are not expected to

300 scale with the attachment efficiency in the analytical solution of the Smoluchowski

301 model which is assumed to be one, we tried to fit the modified CRMs to the analytical

302 solution by adjusting Λ_S and Λ_C as free parameters. Over 100 min aggregation, within a

303 fairly broad range of conditions, i.e., varying q within 1-3, D_f within 1.5-2.5, primary

304 particle size, a_0, between 200 and 300 nm, and initial concentration, C_0, between 10 and

305 50 mg/L, which were totally 99 cases, the S-CRM was able to fit the total number of

306 particles produced by the analytical solution (assuming $\alpha = 1$) very well with a mean

307 *NSE* of 0.990±0.01 (Table S1). In a similar condition, but with a_0 range of 300 and 400

308 nm, and C_0 range of 1 and 10 mg/L (99 cases), the C-CRM was able to fit the analytical

309 solution with a lower mean *NSE* 0.804±0.230 compared to that of S-CRM (Table S2). It

310 appears that fractal dimension is the most sensitive factor in controlling the C-CRM

311 goodness-of-fit. Using C-CRM, an increase in D_f, reduces *NSE* significantly whereas

312 using S-CRM, an increase in D_f elevates *NSE*. The results for the aggregation rate

313 constants for S-CRM and C-CRM fitted to analytical solution outputs are shown in Figs.

314 S1 and S2. These results indicate that aggregation rate constants vary with factors that

315 can affect the particle size distribution grid, i.e., q, D_f, and a_0, and parameters which can

15

316　impact the collision frequency, i.e., C_0. The reason for such behaviours is not clear

317　although they can arise from numerical difficulties at very high aggregation rates

318　required to synchronize the numerical model with the assumption of $\alpha = 1$ in the

319　analytical solution as well as simplifying basic assumptions of the analytical solution

320　such as collision frequency being described only by Brownian collisions. Overall, these

321　results suggest that the modified CRM is able to describe the aggregation phenomenon

322　in most of cases when compared to a simplified analytical solution.

4.2　Experimental results

324　　　The results of hydrodynamic size evolution and DCR are presented in Figs. 1 and

325　2. The late stage of aggregation/sedimentation, i.e., where the slope of size versus time

326　changes significantly, does not appear within 5 h for electrolyte concentrations ≤ 0.5 mM

327　$CaCl_2$ and ≤ 20 mM $NaClO_4$ at pH 6 (reaction limited regime, RLA) whereas above

328　these thresholds the late stage appears as a significant reduction in the slope of the D_H

329　curve versus time. Likewise, at pH <6 and 20 mM $NaClO_4$, the late stage of aggregation

330　appears in D_H curves. These are in general agreement with aggregation trends of

331　hydroxyapatite (HAp) NP observed in the previous study [40]. It appears that critical

332　coagulation concentration (CCC) [81] above which the system is considered under the

333　diffusion limited regime (DLA), is between 0.5-1 mM for $CaCl_2$ and between 30-50 mM

334　for $NaClO_4$. Considering matched D_H curves for SGO size evolution at 0.5 $CaCl_2$ and 30

335　mM $NaClO_4$, CCC ration of monovalent to divalent electrolyte is estimated to be in the

336　range of 50–60 which is within the range calculated by Schulze-Hardy rule, i.e., 4–64

337　[81] and in agreement with ratios measured for GO elsewhere [82]. Considering the

338　proportionality of CCC with $\zeta^4 z^{-2}$ (where ζ is zeta potential and z is valence of the

339　electrolyte) one can also calculate the CCC ration of monovalent to divalent electrolyte

16

340 [83, 84]. According to the zeta potential data, given in Fig. S3, ζ ranges from -25.7 to -

341 19.9 mV for monovalent and from -17.6 to -7.2 for divalent electrolytes at their

342 corresponding CCC ranges assumed above. This yields CCC ration of monovalent to

343 divalent electrolyte from 5.9 to 20.3 which is still within the boundaries of the Schulze-

344 Hardy rule but lower than the ranges calculated above. There is an ongoing research to

345 understand such discrepancies [83-86].

346   At moderate concentration of $CaCl_2$ (0.5 mM), DCR/DCR_0 demonstrates

347 significant increase over time whereas at 30 mM $NaClO_4$, DCR/DCR_0 tends to show a

348 mild decreasing trend (Fig. 1d,e). The increase in DCR/DCR_0 is similar to the previous

349 observations of Babakhani et al. [40], for HAp NP in presence of 0.3 mM $CaCl_2$ at pH 6

350 (RLA regime). Nevertheless, this behaviour seems to be specific to the presence of

351 $CaCl_2$ since this is not noticeable at 30 mM $NaClO_4$ although a slight rise in DCR/DCR_0

352 is observed for lower $NaClO_4$ concentrations—5 and 10 mM (Fig. 1d,e). While in a

353 high-rate aggregating system variation in DCR/DCR_0 may represent the variation in the

354 normalized concentration (C/C_0) of NP, at a low-rate aggregating system DCR/DCR_0

355 may not be a proper indicator of NP C/C_0. This is because in this regime the

356 sedimentation is not significant and C/C_0 is expected to be constant while DCR/DCR_0,

357 especially in presence of $CaCl_2$, demonstrates an increase above unity which might be an

358 impact of scattered light being dependent on particle size, and appearing only when the

359 change in concentration due to sedimentation is not significant. It should be noted that

360 the use of DCR/DCR_0 as a representative of mass concentration in high-rate aggregation

361 systems or DLA conditions was verified in the previous study [40] by being described

362 with a size-matched model. Additionally, when there is no aggregation in the system

363 SGO used in the present study shows a linear correlation between mass concentration

364 and DCR data with a goodness-of-fit coefficient $r^2 = 0.952$ and P value $\gg 0.05$ with the

17

365 null hypothesis being significant difference if $P < 0.05$ (Fig. S4, Supporting

366 Information). Nevertheless, the dependency of the scattered light intensity on the particle

367 size is theoretically proportional to the third power, in contrast to its dependency on

368 mass concentration which is linear [87]. Thus, in an aggregating system in which the size

369 grows over time, DCR's proportionality to mass concentration may not necessarily

370 follow a linear trend. Overall, the reason for the rise of DCR/DCR_0 above unity in a

371 slow-aggregation regime under some solution chemistries is not clear in the scope of the

372 present study, and the real proportionality of DCR on mass concentration in an

373 aggregating system is also not clear currently. These may be addressed in future studies.

374 4.3 Model fit results

375 Nash–Sutcliffe model efficiencies for different model fits to D_H data are shown in Table

376 1 and modelled curves versus observations of D_H and DCR are illustrated in Figs. 1 and

377 2. On average, FP, S-CRM, and C-CRM, show close mean NSE to D_H curves with, 0.29,

378 0.33, and 0.36, respectively. The reason for low overall mean NSE values is that in cases

379 where observation data are close to their mean, i.e., at low aggregation rates such as

380 cases at low electrolyte concentrations of 0.1 mM $CaCl_2$ and 5 mM $NaClO_4$ or at high

381 pH of 10, even though visually a good match is obtained between the two graphs of the

382 observation and modeled data, NSE is not reaching a value close to one as expected, and

383 instead show values close to zero.

384 Based on visual assessment of the fittings, the performance of S-CRM method is slightly

385 poorer than other methods in terms of reproducing the sudden change in D_H gradient

386 between early and late stages of aggregation under the DLA regime (1 mM $CaCl_2$ and 50

387 mM $NaClO_4$, Fig. 1b,c). It seems S-CRM and FP are less capable of mimicking the

388 straight log linear curve of D_H under the RLA regime (0.5 mM $CaCl_2$ and 30 mM

18

NaClO$_4$) than C-CRM method which also reproduces well the change of D_H slope under the DLA regime. This is consistent with the maximum mean *NSE* obtained for the C-CRM.

Considering the DCR data (Figs. 1d,e,f and Fig. 2b), none of models reproduces the rising behaviour of DCR curves at intermediate IS because the simple explicit decay sedimentation term employed in this study is not expected to reproduce increase in the concentration. It should be noted that such a sedimentation model, which does not involve a partial derivative in respect to depth, is simple and does not require spatial discretization in the numerical solution thereby bypassing some of numerical issues/restrictions. However, it is still not clear to what extent the depth profiles resulted from this model match the reality, which is a subject of future studies. Within the DLA regime, all models can, to some extent, reproduce the nonlinear reduction in normalized DCR. In describing DCR trends within this regime, FP technique appeared to perform best followed by S-CRM and C-CRM (Fig. 1d,e,f and Fig. 2b).

Model-produced PSDs based on D_H and DCR-matched models are shown in Figs. 3 and S5. It appears that none of the models can reproduce the PSD in all cases. In most of the cases, both modified CRM approaches tend to preserve the initial position of the PSD over time, although the heights of the peaks are changing. This is more noticeable for the C-CRM than S-CRM. The fixed pivot approach exhibiting considerable movement of the PSD position, appears to overestimate the experimental PSD, and cannot reproduce the stationary stage of the PSD, especially toward the late stage of aggregation. It is possible that in the case of CRM the mass gradually moves to larges size classes and becomes subject to sedimentation before it appears as movement of the PSD. Such a steady-state or equilibrium condition of the PSD has frequently been used as a basic assumption in model developments [24, 88-90]. Although FP overtimes the

19

414 position of PSD, it can reproduce the overall shape of the observed PSD generally better

415 than other methods. On average, in terms of reproducing both shape and position of

416 PSD, the size-based CRM performs relatively better than the other two methods because

417 it produces PSDs with closer positions to observed PSDs, than that produced by FP and

418 with a closer shape to observed PSD than that resulted by C-CRM (Figs. 3 and S5). It

419 should be noted that particle size measurement using DLS for polydisperse samples has

420 been criticized for being affected by the larger size fraction of the size spectrum, because

421 the scattered light intensity is proportional to the size by a power of six [87]. Such

422 uncertainties in the measurement approach makes it complex to find a model which

423 reproduces all aspects of PSD.

424 ## 4.4   Estimated parameter trends

425 The trends of estimated parameters including aggregation rate constants (Λ_S, Λ_C, or α)

426 and fractal dimension, D_f, are shown in Fig. 4 for different solution chemistries.

427 According to this figure, the trends of aggregation rate constants are consistent among all

428 cases. Unlike HAp NPs in a previous study [40], which exhibited multimodal trends of α

429 estimated using the FP method with IS, here FP-estimated values of α for SGO show a

430 positive log linear trend with IS with $r^2=0.93$ and 0.97 for $NaClO_4$ and $CaCl_2$,

431 respectively (Fig. 4a,b) and a negative semi-log linear trend with pH with $r^2 = 0.98$ (Fig.

432 4c). Interestingly, consistent with the trends of α, the CRM-estimated aggregation

433 constants Λ_S and Λ_C display a positive log linear trend with IS ($r^2=0.84$ for C-CRM and

434 $r^2=0.85$ for S-CRM in $NaClO_4$ solution and $r^2=1.00$ for both C-CRM and S-CRM in

435 $CaCl_2$ solution) and a negative semi-log linear trend with pH ($r^2=0.73$ for C-CRM and

436 $r^2=0.86$ for S-CRM). The gradients of the lines fitted to Λ_S and Λ_C versus IS and pH

437 match very well with that of α ($P=0.55$ and $0.61 \gg 0.05$) (Fig. 4a-c).

20

438   Fractal dimension generally increases with IS (Fig. 4d,e) and decreases with pH

439   (Fig. 4f), which is in agreement with Chowdhury et al. [91] measuring D_f for TiO_2 NP

440   using static light scattering (SLS). Yet unlike aggregation constant patterns, D_f trends are

441   not effectively linear (Fig. 4d-f). This is mostly because of large D_f values determined at

442   lowest IS which emanates from the fact that at the lowest IS, the aggregation is not

443   operative and therefore particles remain in their primary size which should have a

444   geometry close to Euclidian thereby having a D_f close to 3 [40]. Estimated D_f in the

445   present study yields close ranges for the three models, namely, from 1.50 to 2.86 for the

446   FP model, from 1.48 to 2.80 for C-CRM, and from 1.70 to 2.70 for S-CRM. Large

447   values of D_f (2.27-2.8) were commonly determined at high IS (DLA regime) while low

448   D_f values (1.48-1.99) were estimated at intermediate IS (RLA regime). Although similar

449   ranges for D_f under DLA have frequently been reported [62, 92], this is opposite to

450   common ranges of D_f, reported for aggregates formed in controlled condition where they

451   are not subject to restructuring, i.e., D_f close to 2.2 within RLA regime and close to 1.7

452   within the DLA regime [46, 71, 91, 93]. The underlying reason for D_f values differing

453   from common ranges is attributed to restructuring of aggregates at greater depths during

454   the late stage of aggregation in quiescent condition [40] as the typical trends and ranges

455   of D_f were achieved when the FP model was fitted only to the early stage of aggregation,

456   or when the measurement depth was reduced to just below the surface of the water

457   column.

458   Overall, the general consistency of parameter trends suggests that CRM model

459   parameters although do not scale with those of FP approach, generally show similar

460   trends with FP parameters in respect to physical factors such as electrolyte concentration

461   and pH. Aggregation rate parameters can be considered variable with size in order to

462   include the impact of solution chemistry such as zeta potential and ionic strength through

21

463 the DLVO theory in a forward prediction mode similar to the previous study [40]. This is

464 beyond the scope of the present study which aims to test the ability of CRM in

465 'describing', rather than 'predicting', the aggregation behavior of NP.

4.5   Comparison of model efficiency and accuracy

467 The results of model run time and mass balance error for every case simulating an

468 experimental duration of 18000 s are reported in Table 2. The computational times vary

469 widely among experimental cases due to different aggregation rates, initial PSDs, etc.

470 The mean runtime for the FP technique is 6.14 min. While it is complicated to compare

471 runtimes across different studies due to differences in computer systems, software

472 versions, number of grid points, simulation duration, initial conditions, etc., considering

473 the simulation duration in the present study (18000 s), it appears that these runtimes for

474 the FP method are comparable with elsewhere [22, 53, 54].

475   Interestingly, the modified CRMs turn out to be about one order-of-magnitude

476 faster than the FP method with mean runtimes 0.92±1.15 min for C-CRM and 0.49±0.53

477 min, for S-CRM. The FP technique is a widely-accepted population-balance model [53,

478 94], with an ability to preserve the two properties, population and mass. The MATLAB

479 code for solving this model was already verified against analytical solutions of the

480 population balance given for different initial conditions [40]. Here the FP method which

481 is inherently a PBM yields a fairly low average absolute mass balance error (3.9×10^{-2}

482 %). However, the proposed models of the present study which are inherently mass-

483 balance models show even lower absolute mass balance errors; 4.2×10^{-6} % and 1.1×10^{-5}

484 %, for C-CRM and S-CRM models, respectively, suggesting that the use of mass balance

485 in modelling aggregation not only leads to a more efficient simulation but also enhances

486 the accuracy.

22

487   It should be noted that based on the current formulation of CRM models, the

488   outcomes might be dependent on the particle size grid configuration such as the

489   maximum number of size classes. A maximum number of 100 size classes may be

490   recommended as a standard that is sufficient to capture PSD evolutions in the

491   environmental systems, and thus this can be fixed as part of the model. We further

492   investigated the influence of the number of size classes on model results. The outcomes

493   presented in Figs. S6 and S7, revealed that at high aggregation rates the dependency on

494   the number of bins is not significant for both C-CRM and S-CRM while at low

495   aggregation rates this dependency is considerable. Further, we fitted the S-CRM model

496   to the analytical solution results of the Smoluchowski model. As shown in Fig. S8, this

497   investigation revealed that there is a log linear relationship between the adjusted S-CRM

498   rate constant and the number of size classes in all cases, suggesting that the impact of

499   number of size classes may be offset from aggregation rate constants in future studies.

500   As already mentioned in Section 4.1 the impact of variation in particle size grid

501   configuration causing changes in the aggregation constant fitted to the analytical solution

502   might also arise from simplifying assumptions of the analytical solution and possible

503   numerical inaccuracies of any given numerical approaches in certain configurations of

504   the particle size grid [40, 53]. Such factors can deviate the trends of aggregation

505   constants of numerical models from that of analytical approach whereas consistent

506   trends are obtained across different numerical methods.

5   Conclusions

508   In this study we propose a new modelling framework based on a mass-balance chain

509   reaction formulation. This includes a series of first-order, coupled decay reaction

510   expressions with mass concentration as the main variable. Two simplifying approaches

23

based on size (S-CRM) or collision frequencies (C-CRM) were proposed for considering variations in the decay-reaction rates in terms of aggregate size classes. The two CRM approaches both can generally fit well to analytical solutions of the aggregation model with a log normal initial PSD within a range of conditions. When fitting to a range of experimental data for early and late aggregation and sedimentation of SGO, the performances of both approaches were generally similar to or better than that of the FP model which is a standard PBE. The new modelling framework was found on average one order-of-magnitude faster than the FP method while yielding a lower average mass balance error. In contrast to FP, modified CRM approaches tended to show a steady-state or equilibrium condition for the shape of the PSD at moderate or low aggregation rates. Similar trends for aggregation rate constants, estimated from model fitting to experimental data, were obtained for all models, and close ranges were obtained for fractal dimensions, suggesting that model parameters for the proposed modified CRM are meaningful and may follow conventional models. Although future studies may present more accurate relationships for CRM reaction rate and yield coefficients, the use of two simplifying/empirical preliminary approaches in this study for reaction rates demonstrated generally similar performances suggesting that the model is not much sensitive to these coefficients and therefore the simplifying assumptions taken in developing current relationships may not affect the model outcomes significantly.

While there are uncertainties in the experimental results, parameter calibration process, and the basic assumptions of model relationships, based on the overall agreement between the modified CRM and analytical/numerical solutions of PBE as well as experimental data of SGO aggregation we conclude that a CRM formulation is able to describe NP aggregation phenomenon. Owing to its flexibility in formulation, low computational expenses, and the use of mass concentration, the CRM may also offer

536 potentials for modelling aggregate breakage, e.g., using negative rate coefficients [24],

537 and may be a suitable option to be modified for modelling hetero-aggregation of NP with

538 background colloids as well as the adsorption of other solute contaminants. The CRM

539 can be a useful approach not only for modelling the aggregation of engineered NP in

540 environmental media, but also for modelling the aggregation of particulate species in

541 other contexts such as biogeochemistry where the complex network of the reactions in

542 the reactive transport model makes incorporation of population balance models

543 computationally cumbersome if possible at all. Overall, this study demonstrates that a

544 chain-reaction model widely used for describing chemical and nuclear reactions can be

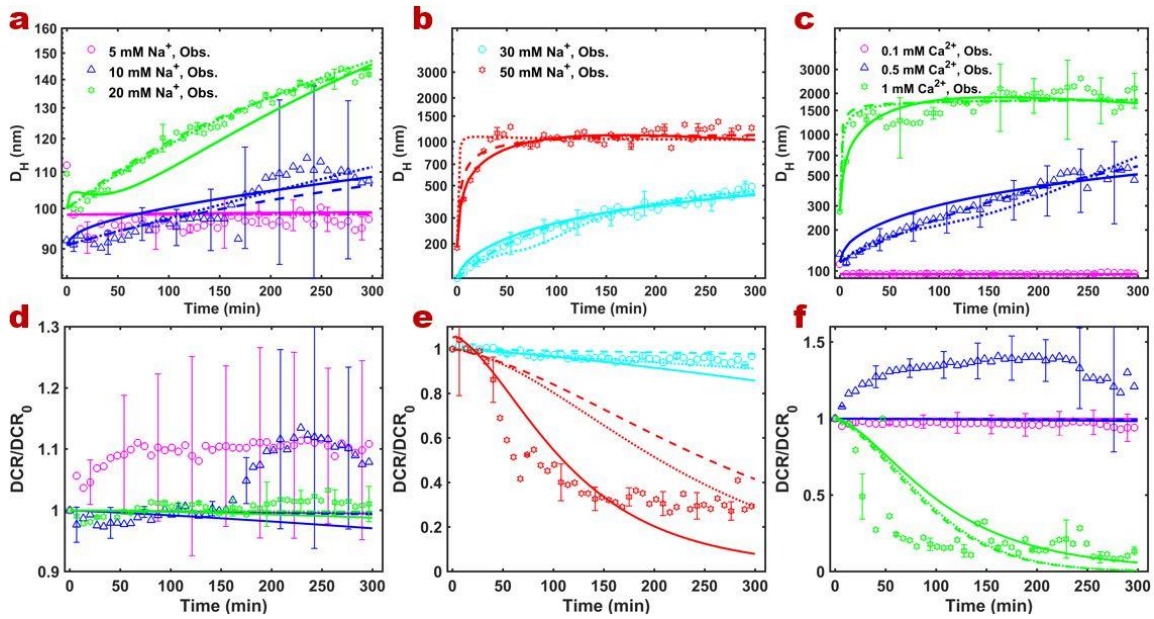545 used for modelling aggregation of colloidal particle.

546

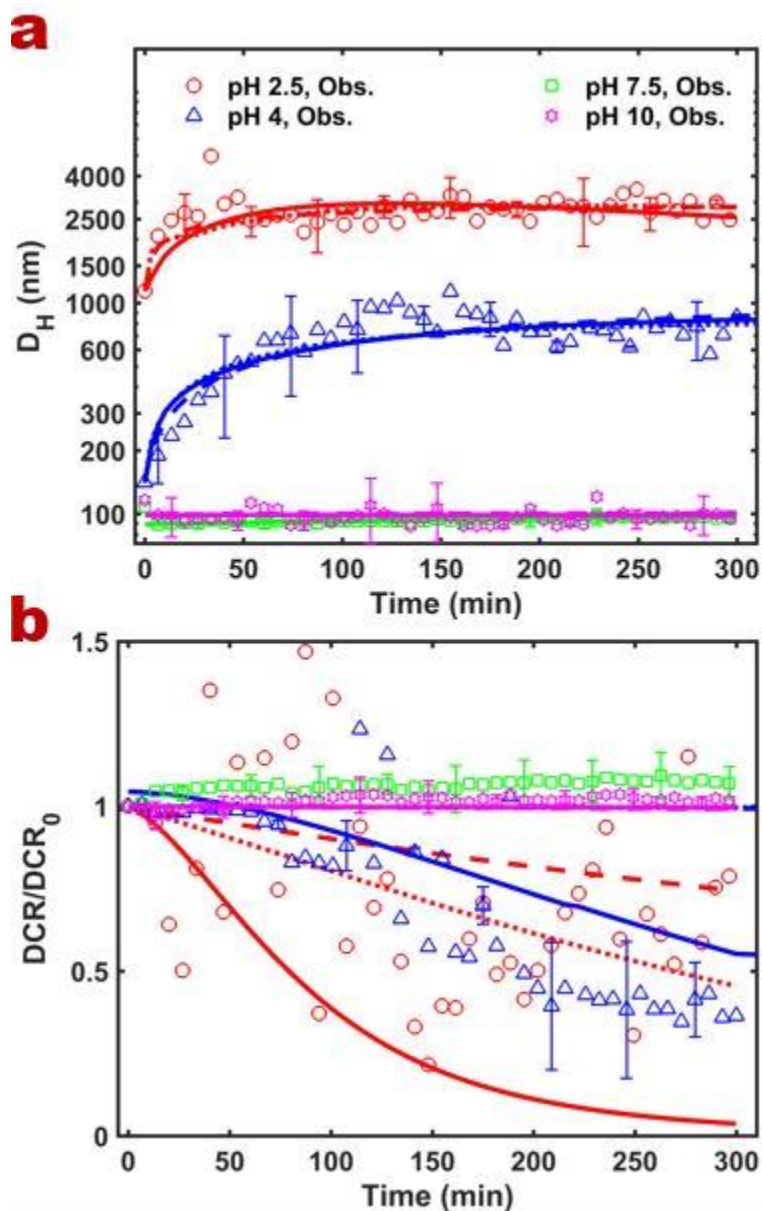556

557

558 **Figure Captions.**

25

Figure 1. Evolutions of size (a-c) and change in normalized derived count rate (DCR/DCR$_0$), (d-f) for SGO NPs in electrolyte species NaClO$_4$ (a,b,d,e) and CaCl$_2$ (c,f) with a fixed pH at 6. Continuous lines represent FP, dash lines represent C-CRM technique, and dot lines represent the S-CRM model outcomes.

564

Figure 2. Evolutions of Size (a) and change in normalized derived count rate (DCR/DCR$_0$), (b) for SGO NPs at various pH with a fixed IS at 20 mM NaClO$_4$. Continuous lines represent FP; dash lines represent C-CRM technique, and dot lines represent the S-CRM model outcomes.
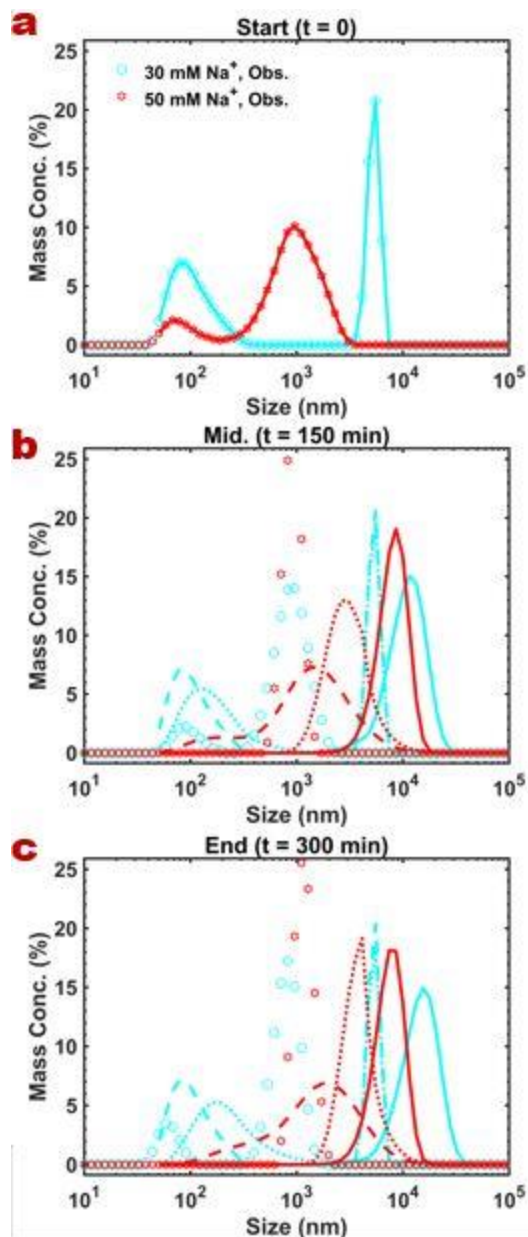
Figure 3. Comparisons of PSD for SGO NPs at 30 and 50 mM $NaClO_4$ with a fixed pH at 6 and at the middle (t=150 min, b) and the end of experiments (t=300 min, c). Continuous lines represent FP; dash lines represent C-CRM technique, and dot lines represent the S-CRM model outcomes. It should be noted that lines in panel (a) only show the initial condition of the model.

28
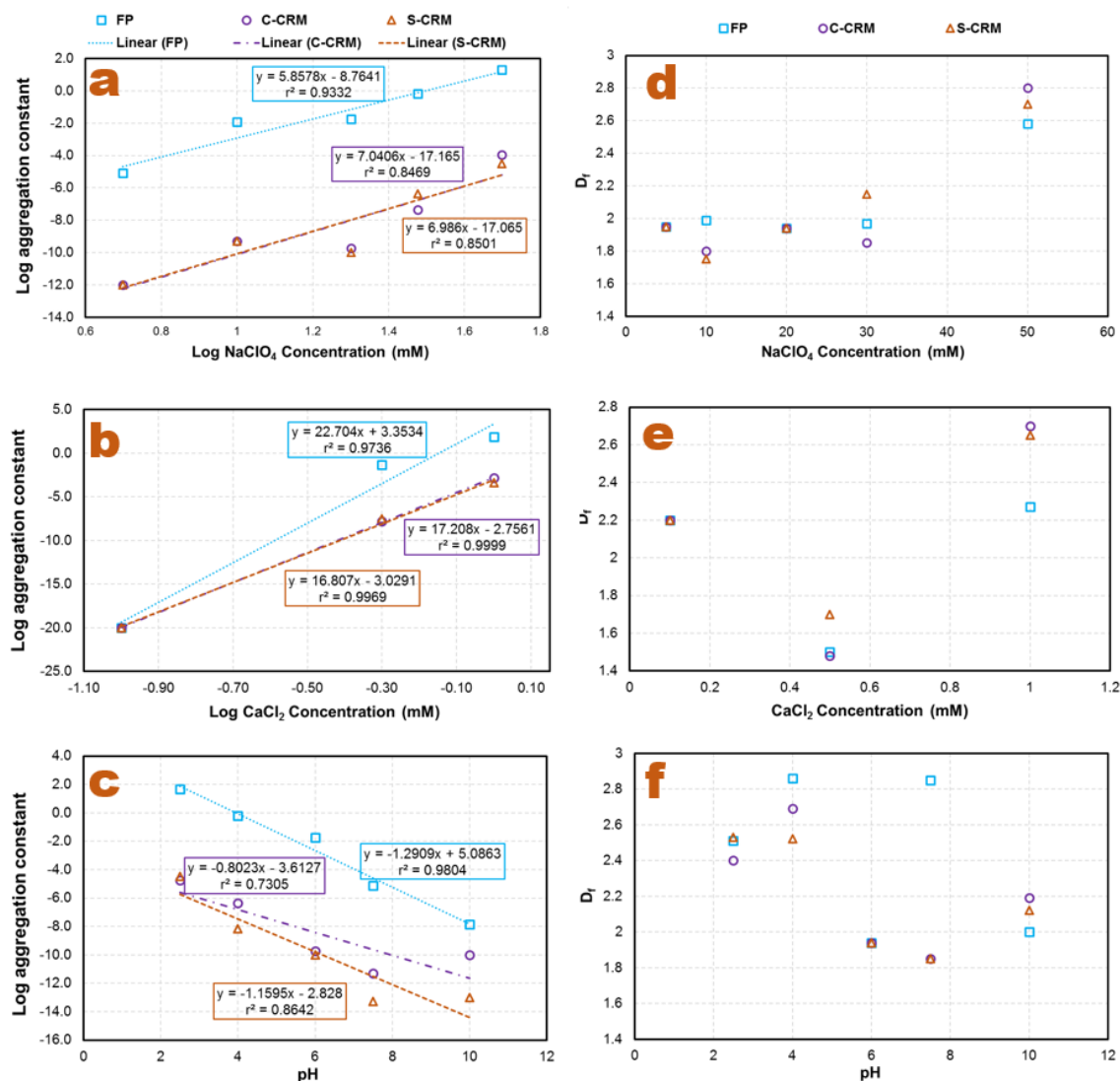
Figure 4. Estimated parameter trends for different models: aggregation rate constants (α, Λ_S, and Λ_C for FP, S-CRM, and C-CRM approaches), vs electrolyte concentration (a,b), and vs pH (c), and fractal dimension, D_f, vs electrolyte concentration (d,e) and vs pH (f).

29

583 **Table 1.** Nash-Sutcliff determination coefficient, NSE, for fittings to hydrodynamic

584 diameter data with different models across various solution chemistries.

pH	Electrolyte concentration	FP	C-CRM	S-CRM
6	0.1 mM $CaCl_2$	-0.093	-0.092	-0.092
	0.5 mM $CaCl_2$	0.862	0.947	0.830
	1 mM $CaCl_2$	0.505	0.340	0.422
	5 mM $NaClO_4$	-1.141	-0.826	-0.843
	10 mM $NaClO_4$	0.683	0.694	0.842
	20 mM $NaClO_4$	0.827	0.978	0.971
	30 mM $NaClO_4$	0.923	0.940	0.912
	50 mM $NaClO_4$	0.447	0.587	0.178
2.5	20 mM $NaClO_4$	-0.245	0.067	-0.072
4		0.492	0.488	0.537
7.5		0.257	0.256	0.255
10		0.000	-0.033	0.000

585

586

587

588

589

590

Table 2. Comparison of the model run times and mass balance errors in a single-run

mode based on parameters estimated from the calibration process.

pH	Electrolyte concentration	Model Run Time (min)	Mass balance error (%)	Model Run Time (min)	Mass balance error (%)	Model Run Time (min)	Mass balance error (%)
		FP		**C-CRM**		**S-CRM**	
6	0.1 mM CaCl$_2$	3.77	-7.1E-14	0.06	-2.8E-14	0.04	-2.8E-14
	0.5 mM CaCl$_2$	0.60	-2.1E-04	0.28	5.3E-10	0.04	9.4E-11
	1 mM CaCl$_2$	1.23	-4.1E-01	2.22	-9.5E-06	1.48	-9.1E-05
	5 mM NaClO$_4$	30.06	1.1E-08	0.13	-2.8E-14	0.09	1.4E-14
	10 mM NaClO$_4$	0.94	-2.9E-05	0.29	-1.0E-08	0.20	-1.5E-08
	20 mM NaClO$_4$	5.99	-3.8E-05	0.66	2.1E-11	0.47	8.4E-13
	30 mM NaClO$_4$	1.32	-2.4E-05	0.27	-4.7E-06	0.18	-5.0E-06
	50 mM NaClO$_4$	4.73	-5.1E-02	2.08	-3.6E-05	1.34	-3.8E-05
2.5	20 mM NaClO$_4$	2.59	4.4E-07	1.03	1.9E-08	0.70	2.5E-09
4		18.17	-3.9E-07	3.67	1.1E-13	1.10	2.8E-14
7.5		0.46	3.1E-12	0.07	-2.7E-08	0.05	-1.0E-08
10		3.87	4.0E-12	0.22	3.0E-13	0.12	-1.4E-14

599   **References**

600   [1] A. Zurutuza, C. Marinelli, Challenges and opportunities in graphene commercialization,
601   Nature nanotechnology, 9 (2014) 730.

602   [2]   Nanotechnology-Products-Database,
603   http://product.statnano.com/search?keyword=graphene+oxide, 2018.

604   [3] A.A. Keller, S. McFerran, A. Lazareva, S. Suh, Global life cycle releases of engineered
605   nanomaterials, J. Nanopart. Res., 15 (2013) 1-17.

606   [4] J. Zhao, Z. Wang, J.C. White, B. Xing, Graphene in the aquatic environment: adsorption,
607   dispersion, toxicity and transformation, Environmental science & technology, 48 (2014)
608   9995-10009.

609   [5] A.Y. Romanchuk, A.S. Slesarev, S.N. Kalmykov, D.V. Kosynkin, J.M. Tour, Graphene
610   oxide for effective radionuclide removal, PCCP, 15 (2013) 2321-2327.

611   [6] S. Yu, X. Wang, X. Tan, X. Wang, Sorption of radionuclides from aqueous systems onto
612   graphene oxide-based materials: a review, Inorganic Chemistry Frontiers, (2015).

613   [7] S.S. Patil, U.U. Shedbalkar, A. Truskewycz, B.A. Chopade, A.S. Ball, Nanoparticles for
614   environmental clean-up: a review of potential risks and emerging solutions,
615   Environmental Technology & Innovation, 5 (2016) 10-21.

616   [8] C.M. Park, D. Wang, C. Su, Recent Developments in Engineered Nanomaterials for Water
617   Treatment and Environmental Remediation, Handbook of Nanomaterials for Industrial
618   Applications, Elsevier2018, pp. 849-882.

619   [9] M. Kah, R.S. Kookana, A. Gogos, T.D. Bucheli, A critical evaluation of nanopesticides and
620   nanofertilizers against their conventional analogues, Nature nanotechnology, (2018) 1.

621   [10] C.O. Dimkpa, P.S. Bindraban, Nanofertilizers: New products for the industry?, J. Agric.
622   Food. Chem., (2017).

623   [11] H. Ehtesabi, M.M. Ahadian, V. Taghikhani, M.H. Ghazanfari, Enhanced heavy oil recovery
624   in sandstone cores using tio2 nanofluids, Energy & Fuels, 28 (2013) 423-430.

625   [12] N.H. Pham, D.V. Papavassiliou, Hydrodynamic effects on the aggregation of nanoparticles
626   in porous media, Int. J. Heat Mass Transfer, 121 (2018) 477-487.

627   [13] P.M. Abraham, S. Barnikol, T. Baumann, M. Kuehn, N.P. Ivleva, G.E. Schaumann,
628   Sorption of silver nanoparticles to environmental and model surfaces, Environmental
629   science & technology, 47 (2013) 5083-5091.

630   [14] C. Nickel, S. Gabsch, B. Hellack, A. Nogowski, F. Babick, M. Stintz, T.A.J. Kuhlbusch,
631   Mobility of coated and uncoated TiO 2 nanomaterials in soil columns−Applicability of
632   the tests methods of OECD TG 312 and 106 for nanomaterials, Journal of environmental
633   management, 157 (2015) 230-237.

634   [15] P. Babakhani, J. Bridge, T. Phenrat, R.-a. Doong, K. Whittle, Aggregation and
635   sedimentation of shattered graphene oxide nanoparticles in dynamic environments: a
636   solid-body   rotational   approach,   Environmental   Science: Nano,   doi:
637   10.1039/C8EN00443A (2018).

638   [16] E.M. Hotze, T. Phenrat, G.V. Lowry, Nanoparticle Aggregation: Challenges to
639   Understanding Transport and Reactivity in the Environment, J. Environ. Qual., 39
640   (2010) 1909–1924.

641   [17] T. Phenrat, H.J. Kim, F. Fagerlund, T. Illangasekare, R.D. Tilton, G.V. Lowry, Particle size
642   distribution, concentration, and magnetic attraction affect transport of polymer-modified
643   Fe0 nanoparticles in sand columns, Environ. Sci. Technol., 43 (2009) 5079-5085.

32

644 [18] T. Phenrat, H.-J. Kim, F. Fagerlund, T. Illangasekare, G.V. Lowry, Empirical correlations to
645   estimate agglomerate size and deposition during injection of a polyelectrolyte-modified
646   Fe0 nanoparticle at high particle concentration in saturated sand, J. Contam. Hydrol., 118
647   (2010) 152-164.

648 [19] T. Phenrat, N. Saleh, K. Sirk, R.D. Tilton, G.V. Lowry, Aggregation and sedimentation of
649   aqueous nanoscale zerovalent iron dispersions, Environmental Science & Technology,
650   41 (2007) 284-290.

651 [20] T. Phenrat, G.V. Lowry, Nanoscale Zerovalent Iron Particles for Environmental
652   Restoration, Springer2019.

653 [21] T. Raychoudhury, N. Tufenkji, S. Ghoshal, Aggregation and deposition kinetics of
654   carboxymethyl cellulose-modified zero-valent iron nanoparticles in porous media, Water
655   Res., 46 (2012) 1735-1744.

656 [22] A.L. Dale, G.V. Lowry, E.A. Casman, Accurate and fast numerical algorithms for tracking
657   particle size distributions during nanoparticle aggregation and dissolution,
658   Environmental Science: Nano, 4 (2017) 89-104.

659 [23] A.L. Dale, G.V. Lowry, E.A. Casman, Much ado about α: reframing the debate over
660   appropriate fate descriptors in nanoparticle environmental risk modeling, Environmental
661   Science: Nano, (2015).

662 [24] P. Babakhani, F. Fagerlund, A. Shamsai, G.V. Lowry, T. Phenrat, Modified MODFLOW-
663   based model for simulating the agglomeration and transport of polymer-modified Fe
664   nanoparticles in saturated porous media, Environ Sci Pollut Res, 1-20,
665   doi:10.1007/s11356-015-5193-0, (2018).

666 [25] P. Babakhani, J. Bridge, R.-a. Doong, T. Phenrat, Continuum-based models and concepts
667   for the transport of nanoparticles in saturated porous media: A state-of-the-science
668   review, Adv. Colloid Interface Sci., 246 (2017) 75-104.

669 [26] C.D. Tsakiroglou, A. Sikinioti-Lock, K. Terzi, M. Theodoropoulou, A numerical model to
670   simulate the NAPL source zone remediation by injecting zero-valent iron nanoparticles,
671   Chem. Eng. Sci., 192 (2018) 391-413.

672 [27] L.M. Gilbertson, B.A. Wender, J.B. Zimmerman, M.J. Eckelman, Coordinating modeling
673   and experimental research of engineered nanomaterials to improve life cycle assessment
674   studies, Environmental Science: Nano, 2 (2015) 669-682.

675 [28] L. Pourzahedi, M. Pandorf, D. Ravikumar, J.B. Zimmerman, T.P. Seager, T.L. Theis, P.
676   Westerhoff, L.M. Gilbertson, G.V. Lowry, Life cycle considerations of nano-enabled
677   agrochemicals: are today's tools up to the task?, Environmental Science: Nano, 5 (2018)
678   1057-1069.

679 [29] A.A. Keller, A. Lazareva, Predicted releases of engineered nanomaterials: from global to
680   regional to local, Environmental Science & Technology Letters, 1 (2013) 65-70.

681 [30] N.C. Mueller, B. Nowack, Exposure modeling of engineered nanoparticles in the
682   environment, Environmental science & technology, 42 (2008) 4447-4453.

683 [31] D. Mackay, E. Webster, I. Cousins, T. Cahill, K. Foster, T. Gouin, An introduction to
684   multimedia models, CEMC Report, (2001) 30.

685 [32] B. Nowack, M. Baalousha, N. Bornhöft, Q. Chaudhry, G. Cornelis, J. Cotterill, A.
686   Gondikas, M. Hassellöv, J. Lead, D.M. Mitrano, Progress towards the validation of
687   modeled environmental concentrations of engineered nanomaterials by analytical
688   measurements, Environmental Science: Nano, (2015).

689 [33] T. Phenrat, F. Fagerlund, T. Illangasekare, G.V. Lowry, R.D. Tilton, Polymer-Modified Fe0
690   Nanoparticles Target Entrapped NAPL in Two Dimensional Porous Media: Effect of

33

Particle Concentration, NAPL Saturation, and Injection Strategy, Environmental Science & Technology, 45 (2011) 6102-6109.

[34] F. Fagerlund, T.H. Illangasekare, T. Phenrat, H.J. Kim, G.V. Lowry, PCE dissolution and simultaneous dechlorination by nanoscale zero-valent iron particles in a DNAPL source zone, J. Contam. Hydrol., 131 (2012) 9-28.

[35] H.-J. Kim, T. Phenrat, R.D. Tilton, G.V. Lowry, Effect of kaolinite, silica fines and pH on transport of polymer-modified zero valent iron nano-particles in heterogeneous porous media, J. Colloid Interface Sci., 370 (2012) 1-10.

[36] S.M. Louie, R.D. Tilton, G.V. Lowry, Effects of molecular weight distribution and chemical properties of natural organic matter on gold nanoparticle aggregation, Environmental science & technology, 47 (2013) 4245-4254.

[37] S.M. Louie, R.D. Tilton, G.V. Lowry, Critical review: impacts of macromolecular coatings on critical physicochemical processes controlling environmental fate of nanomaterials, Environmental Science: Nano, 3 (2016) 283-310.

[38] A.L. Dale, E.A. Casman, G.V. Lowry, J.R. Lead, E. Viparelli, M. Baalousha, Modeling Nanomaterial Environmental Fate in Aquatic Systems, Environmental Science & Technology, 49 (2015) 2587-2593.

[39] L. He, L. Xie, D. Wang, W. Li, J.D. Fortner, Q. Li, Y. Duan, Z. Shi, P. Liao, C. Liu, Elucidating the Role of Sulfide on the Stability of Ferrihydrite Colloids under Anoxic Conditions, Environmental science & technology, (2019).

[40] P. Babakhani, R.-a. Doong, J. Bridge, Significance of early and late stages of coupled aggregation and sedimentation in the fate of nanoparticles: measurement and modelling, Environmental science & technology, doi: 10.1021/acs.est.7b05236 (2018).

[41] J.T.K. Quik, D. van De Meent, A.A. Koelmans, Simplifying modeling of nanoparticle aggregation–sedimentation behavior in environmental systems: A theoretical analysis, Water Res., 62 (2014) 193-201.

[42] R. Arvidsson, S. Molander, B.A. Sandén, M. Hassellöv, Challenges in exposure modeling of nanoparticles in aquatic environments, Human and Ecological Risk Assessment, 17 (2011) 245-262.

[43] M.R. Soltanian, A. Sun, Z. Dai, Reactive transport in the complex heterogeneous alluvial aquifer of Fortymile Wash, Nevada, Chemosphere, 179 (2017) 379-386.

[44] M. Therezien, A. Thill, M.R. Wiesner, Importance of heterogeneous aggregation for NP fate in natural and engineered systems, Sci. Total Environ., 485 (2014) 309-318.

[45] A.B. Burd, S.B. Moran, G.A. Jackson, A coupled adsorption–aggregation model of the POC/234Th ratio of marine particles, Deep Sea Research Part I: Oceanographic Research Papers, 47 (2000) 103-120.

[46] M. Elimelech, J. Gregory, X. Jia, Particle deposition and aggregation: measurement, modelling and simulation, Butterworth-Heinemann1998.

[47] I. Szilagyi, T. Szabo, A. Desert, G. Trefalt, T. Oncsik, M. Borkovec, Particle aggregation mechanisms in ionic liquids, PCCP, 16 (2014) 9515-9524.

[48] M. Han, D.F. Lawler, The (relative) insignificance of G in flocculation, Journal (American Water Works Association), (1992) 79-91.

[49] K.W. Lee, Y.J. Lee, D.S. Han, The log-normal size distribution theory for Brownian coagulation in the low Knudsen number regime, J. Colloid Interface Sci., 188 (1997) 486-492.

[50] M. Tourbin, C. Frances, Experimental characterization and population balance modelling of the dense silica suspensions aggregation process, Chem. Eng. Sci., 63 (2008) 5239-5251.

[51] S. Kumar, D. Ramkrishna, On the solution of population balance equations by discretization—I. A fixed pivot technique, Chem. Eng. Sci., 51 (1996) 1311-1332.

[52] J. Kumar, M. Peglow, G. Warnecke, S. Heinrich, An efficient numerical technique for solving population balance equation involving aggregation, breakage, growth and nucleation, Powder Technol., 182 (2008) 81-104.

[53] I. Nopens, D. Beheydt, P.A. Vanrolleghem, Comparison and pitfalls of different discretised solution methods for population balance models: a simulation study, Computers & chemical engineering, 29 (2005) 367-377.

[54] A. Majumder, V. Kariwala, S. Ansumali, A. Rajendran, Lattice Boltzmann method for population balance equations with simultaneous growth, nucleation, aggregation and breakage, Chem. Eng. Sci., 69 (2012) 316-328.

[55] S. Bove, T. Solberg, B.H. Hjertager, A novel algorithm for solving population balance equations: the parallel parent and daughter classes. Derivation, analysis and testing, Chem. Eng. Sci., 60 (2005) 1449-1464.

[56] V. Bedekar, E.D. Morway, C.D. Langevin, M.J. Tonkin, MT3D-USGS version 1: A US Geological Survey release of MT3DMS updated with new and expanded transport capabilities for use with MODFLOW, US Geological Survey, 2016.

[57] T.P. Clement, A Modular Computer Code for Simulating Reactive Multispecies Transport in 3-Dimensional Groundwater Systems, The U.S. Department of Energy, (1997) 1-59.

[58] C. Zheng, MT3D99, A Modular 3D Multispecies Transport Simulator User's Guide, SS Papadopulos & Associates Inc, (2000).

[59] M.J. Hounslow, R.L. Ryall, V.R. Marshall, A discretized population balance for nucleation, growth, and aggregation, AIChE J., 34 (1988) 1821-1832.

[60] J. Lister, D. Smit, M. Hounslow, Adjustable discretized population balance for growth and aggregation, AIChE J., 41 (1995) 591-603.

[61] A.A. Markus, J.R. Parsons, E.W.M. Roex, P. de Voogt, R. Laane, Modeling aggregation and sedimentation of nanoparticles in the aquatic environment, Sci. Total Environ., 506 (2015) 323-329.

[62] M.C. Sterling, J.S. Bonner, A.N.S. Ernest, C.A. Page, R.L. Autenrieth, Application of fractal flocculation and vertical transport model to aquatic sol–sediment systems, Water Res., 39 (2005) 1818-1830.

[63] M. Smoluchowski, Versuch einer mathematischen Theorie der Koagulationskinetik kolloider Lösungen, Zeitschrift fuer Physikalische Chemie. 92., 129-68 (1917).

[64] M. Singh, J. Kumar, A. Bück, A volume conserving discrete formulation of aggregation population balance equations on non-uniform meshes, IFAC-PapersOnLine, 48 (2015) 192-197.

[65] S. Chandrasekhar, Stochastic problems in physics and astronomy, Reviews of modern physics, 15 (1943) 1.

[66] J.R. Hunt, Self-similar particle-size distributions during coagulation: theory and experimental verification, J. Fluid Mech., 122 (1982) 169-185.

[67] J.R. Hunt, Particle aggregate breakup by fluid shear, Estuarine cohesive sediment dynamics, Springer1986, pp. 85-109.

[68] M.B. Seymour, G. Chen, C. Su, Y. Li, Transport and Retention of Colloids in Porous Media: Does Shape Really Matter?, Environmental Science & Technology, 47 (2013) 8391-8398.

35

783   [69] B.M. Dolgonosov, Kinetics of sedimentation of a coagulating suspension, Theor. Found.
784   Chem. Eng., 39 (2005) 635-642.

785   [70] S. Veerapaneni, M.R. Wiesner, Hydrodynamics of fractal aggregates with radially varying
786   permeability, J. Colloid Interface Sci., 177 (1996) 45-57.

787   [71] P.J. Vikesland, R.L. Rebodos, J.Y. Bottero, J. Rose, A. Masion, Aggregation and
788   sedimentation of magnetite nanoparticle clusters, Environmental Science: Nano, 3
789   (2016) 567-577.

790   [72] J.E. Nash, J.V. Sutcliffe, River flow forecasting through conceptual models part I — A
791   discussion of principles, Journal of Hydrology, 10 (1970) 282-290.

792   [73] Y. Sun, B. Gao, S.A. Bradford, L. Wu, H. Chen, X. Shi, J. Wu, Transport, retention, and
793   size perturbation of graphene oxide in saturated porous media: Effects of input
794   concentration and grain size, Water Res., 68 (2015) 24-33.

795   [74] L. Liu, B. Gao, L. Wu, Y. Sun, Z. Zhou, Effects of surfactant type and concentration on
796   graphene retention and transport in saturated porous media, Chem. Eng. J., 262 (2015)
797   1187-1191.

798   [75] L. Liu, B. Gao, L. Wu, L. Yang, Z. Zhou, H. Wang, Effects of pH and surface metal
799   oxyhydroxides on deposition and transport of carboxyl-functionalized graphene in
800   saturated porous media, J. Nanopart. Res., 15 (2013) 1-8.

801   [76] B.A. Nordmark, T.M. Przybycien, R.D. Tilton, Comparative coagulation performance study
802   of Moringa oleifera cationic protein fractions with varying water hardness, Journal of
803   Environmental Chemical Engineering, 4 (2016) 4690-4698.

804   [77] S. Xu, B. Gao, J.E. Saiers, Straining of colloidal particles in saturated porous media, Water
805   Resour. Res., 42 (2006).

806   [78] W. Um, R.J. Serne, C.F. Brown, K.A. Rod, Uranium (VI) sorption on iron oxides in
807   Hanford Site sediment: Application of a surface complexation model, Appl. Geochem.,
808   23 (2008) 2649-2657.

809   [79] S.J. Wallace, J. Li, R.L. Nation, B.J. Boyd, Drug release from nanomedicines: selection of
810   appropriate encapsulation and release methodology, Drug delivery and translational
811   research, 2 (2012) 284-292.

812   [80] M. Holmboe, S. Wold, M. Jonsson, S. Garcia-Garcia, Effects of γ-irradiation on the stability
813   of colloidal Na+-Montmorillonite dispersions, Applied Clay Science, 43 (2009) 86-90.

814   [81] K. Afshinnia, M. Sikder, B. Cai, M. Baalousha, Effect of nanomaterial and media
815   physicochemical properties on Ag NM aggregation kinetics, J. Colloid Interface Sci.,
816   487 (2017) 192-200.

817   [82] Y. Jiang, R. Raliya, J.D. Fortner, P. Biswas, Graphene oxides in water: correlating
818   morphology and surface chemistry with aggregation behavior, Environmental science &
819   technology, 50 (2016) 6964-6973.

820   [83] G. Trefalt, I. Szilagyi, G. Téllez, M. Borkovec, Colloidal Stability in Asymmetric
821   Electrolytes: Modifications of the Schulze–Hardy Rule, Langmuir, 33 (2017) 1695-1704.

822   [84] P. Rouster, M. Pavlovic, I. Szilagyi, Destabilization of titania nanosheet suspensions by
823   inorganic salts: Hofmeister series and Schulze-Hardy rule, The Journal of Physical
824   Chemistry B, 121 (2017) 6749-6758.

825   [85] T. Oncsik, G. Trefalt, M. Borkovec, I. Szilagyi, Specific ion effects on particle aggregation
826   induced by monovalent salts within the Hofmeister series, Langmuir, 31 (2015) 3799-
827   3807.

36

828 [86] T. Cao, I. Szilagyi, T. Oncsik, M. Borkovec, G. Trefalt, Aggregation of colloidal particles in
829 the presence of multivalent co-ions: The inverse Schulze–Hardy rule, Langmuir, 31
830 (2015) 6610-6614.

831 [87] J. Shang, X. Gao, Nanoparticle counting: towards accurate determination of the molar
832 concentration, Chem. Soc. Rev., 43 (2014) 7267-7278.

833 [88] S.K. Friedlander, Similarity considerations for the particle-size spectrum of a coagulating,
834 sedimenting aerosol, Journal of Meteorology, 17 (1960) 479-483.

835 [89] J.j. Zhang, X.y. Li, Modeling particle-size distribution dynamics in a flocculation system,
836 AIChE J., 49 (2003) 1870-1882.

837 [90] D.J. Jeffrey, Quasi-stationary approximations for the size distribution of aerosols, Journal of
838 the Atmospheric Sciences, 38 (1981) 2440-2443.

839 [91] I. Chowdhury, S.L. Walker, S.E. Mylon, Aggregate morphology of nano-TiO2: role of
840 primary particle size, solution chemistry, and organic matter, Environmental Science:
841 Processes & Impacts, 15 (2013) 275-282.

842 [92] C. Allain, M. Cloitre, F. Parisse, Settling by cluster deposition in aggregating colloidal
843 suspensions, J. Colloid Interface Sci., 178 (1996) 411-416.

844 [93] J. Zhang, J. Buffle, Multi-method determination of the fractal dimension of hematite
845 aggregates, Colloids and Surfaces A: Physicochemical and Engineering Aspects, 107
846 (1996) 175-187.

847 [94] I. Nopens, P.A. Vanrolleghem, Comparison of discretization methods to solve a population
848 balance model of activated sludge flocculation including aggregation and breakage,
849 Mathematical and Computer Modelling of Dynamical Systems, 12 (2006) 441-454.

850

37